Acta Materialia 163 (2019) 199–207

Contents lists available at ScienceDirect

Acta Materialia

journal homepage: www.elsevier.com/locate/actamat

Full length article

Determination of the structure and properties of an edge dislocation in rutile TiO_2

Emile Maras [a, b], Mitsuhiro Saito [c, d], Kazutoshi Inoue [d], Hannes Jónsson [e], Yuichi Ikuhara [c, d, f], Keith P. McKenna [g, *]

[a] COMP Centre of Excellence, Aalto University School of Science, FI-00076 Aalto, Espoo, Finland
[b] Department of Applied Physics, Aalto University School of Science, FI-00076 Aalto, Espoo, Finland
[c] Advanced Institute for Materials Research, Tohoku University, 2-1-1 Katahira, Aoba-ku, Sendai 980-8577, Japan
[d] Institute of Engineering Innovation, University of Tokyo, 2-11-16, Yayoi, Bunkyo-ku, Tokyo 113-8656, Japan
[e] Science Institute of the University of Iceland, 107 Reykjavík, Iceland
[f] Nanostructures Research Laboratory, Japan Fine Ceramics Center, 2-4-1 Mutsuno, Atsuta-ku, Nagoya 456-8587, Japan
[g] Department of Physics, University of York, Heslington, York YO10 5DD, UK

ARTICLE INFO

Article history:
Received 30 July 2018
Received in revised form
11 September 2018
Accepted 8 October 2018
Available online 9 October 2018

ABSTRACT

A global optimization procedure is used to predict the structure and electronic properties of the $\boldsymbol{b} = c$ [001] edge dislocation in rutile TiO_2. Over 1000 different atomic configurations have been generated using both semi-empirical and density functional theory estimates of the energy of the system to identify the most stable structure. Both stoichiometric and oxygen deficient dislocation core structures are predicted to be stable depending on the oxygen chemical potential. The latter is associated with Ti^{3+} species in the dislocation core. The dislocation is predicted to act as a trap for electrons but not for holes suggesting they are not strong recombination centers. The predicted structures and properties are found to be consistent with experimental results obtained using scanning transmission electron microscopy and electron energy loss spectroscopy on samples produced using the bicrystal approach.

1. Introduction

Dislocations are common defects in semiconducting and insulating materials and their presence can lead to significant modification of mechanical, optoelectronic and chemical properties [1–6]. For example, dislocations (together with segregated point defects) can act as pathways for enhanced electron or ion conductivity as well as sites for the trapping and recombination of photo-excited charge carriers [7–13]. While elemental semiconductors have been well studied both theoretically and experimentally, the variable stoichiometry of compound semiconductors makes predicting and probing their structure considerably more challenging [9,12,14]. Theoretical modeling of associated electronic properties is also more difficult since many widely used approximations give a poor description of the electronic structure of the bulk crystal and associated point defects [15–17]. The oxide semiconductor TiO_2 exemplifies many of these challenges. It has a number of stable and metastable phases (rutile and anatase being the most common and both having band gaps close to 3 eV) and is often oxygen deficient [18,19]. Oxygen vacancies in TiO_2 are known to act as electron donors and in the case of rutile, electrons localize predominantly on Ti ions forming Ti^{3+} sites [20–22]. Importantly standard theoretical approaches (e.g. density functional theory with local or semi-local approximations to exchange and correlation) do not reproduce all of these features. There are also a number of technological applications where dislocations in TiO_2 are suspected to play an important role, including in resistive switching memories, solar cells and photocatalysis [23,24]. Edge dislocations in TiO_2 can be generated by mechanical deformation [25,26], produced during growth of films to accommodate the lattice misfit with the substrate, or formed at interfaces between nanocrystals due to their imperfect oriented attachment [27]. Their effects on both electrical properties and photocatalytic behavior have been studied experimentally [28,29], however the atomic structure and electronic properties of dislocations in TiO_2 remain poorly understood. This presents an obstacle to deeper understanding and materials optimization.

In this article, we employ a multilevel computational modeling

* Corresponding author.
E-mail address: keith.mckenna@york.ac.uk (K.P. McKenna).

https://doi.org/10.1016/j.actamat.2018.10.015

approach to determine the structure and electronic properties of the $\boldsymbol{b} = c[001]$ edge dislocation in rutile TiO_2. First, to identify candidate dislocation structures for a range of stoichiometries, a global optimization approach is used together with a second-moment tight-binding charge equilibration potential to describe interatomic interactions [30–37]. The most stable structures thus obtained undergo subsequent screening using density functional theory (DFT) before the structures and electronic properties of the most stable are evaluated using a DFT + U approach [38]. In this way, the most stable dislocation structures are identified over a range of oxygen chemical potential together with their associated electronic properties. Under reducing conditions, we find that the dislocation is oxygen deficient and associated with electrons that localize on Ti sites near the dislocation core. The predicted structures and electronic properties of the $\boldsymbol{b} = c[001]$ edge dislocation are compared with scanning transmission electron microscopy (STEM) and electron energy loss spectroscopy (EELS) measurements using the bicrystal approach [39]. Despite the challenges involved in imaging this defect experimentally, the calculations are found to be consistent with the experimental measurements. This study demonstrates the feasibility of our multilevel approach for predicting the structure and electronic properties of complex dislocation defects in compound semiconductors. We show that variations in the stoichiometry associated with dislocations in TiO_2 can lead to electron localization near the core. This raises the interesting prospect that one could manipulate site reduction in TiO_2 via control over dislocations (so called dislocation technology [40]) presenting a novel route to engineer electronic properties for catalytic and optoelectronic applications.

2. Methods

2.1. Theoretical modeling

In order to identify promising core configurations, we use the second moment tight binding charge transfer model (SMTBQ) [30–33]. This is a variable-charge model in which the iono-covalent metal-oxygen bond is described by means of the tight-binding formalism for an approximate description of the electronic structure of the oxide. The SMTBQ model is used in combination with a global optimization (GO) algorithm to explore the potential energy surface by finding saddle points [34–37]. The search for a new configuration goes as follows. Starting from a local minimum, atoms close to the dislocation core are slightly displaced in a random way. The minimum mode following method is then used to climb up on the energy surface toward an adjacent saddle point [34,37]. The system is then slightly displaced along the unstable mode away from the initial local minimum and a minimization is carried out to identify the minimum on the other side of the saddle point. By carrying out repeated searches from an initial local minimum, several other local minima are found. One of the new local minima is then selected and new searches from this configuration are carried out (full details of the GO approach are given in Ref. [30]). Configurations are considered identical if they are separated by less than 0.4 Å in phase space *and* if the difference in energy is less than 0.2 eV. The algorithm is essentially a simulated annealing algorithm where new states are identified by finding first order saddle points (transition states) and in that way is analogous to what is done in long time scale dynamics simulations using the adaptive kinetic Monte Carlo method [35]. The EON software was used for these calculations [41]. For the GO search, charge equilibration is turned off. More than 1000 configurations were found. The configurations with lower energy are then relaxed with charge equilibration and the best configurations studied using DFT. All calculations have been performed with charge neutrality. Performing accurate calculations on charged supercells would be extremely challenging due to the periodic boundary conditions and the need to remove artificial interactions with periodic images. We return to discuss whether this is a reasonable approximation in Sec. 4.

DFT calculations are carried out using the projector augmented wave (PAW) method as implemented in the Vienna *ab initio* simulation package (VASP) [42,43]. As a first pre-screening of structures obtained using the SMTBQ based GO method, a spin-polarized DFT calculation is carried out using the generalized gradient approximation (GGA) of Perdew-Burke-Ernzerhof (PBE) to describe exchange and correlation [44]. The 2s and 2*p* electrons of O and the 3d and 4s electrons of Ti are treated as valence electrons and expanded in a plane wave basis with a cutoff energy of 300 eV. For the first level of pre-screening (hereafter referred to as DFT-1) only the gamma point in the Brillouin zone is included and the positions of all atoms are optimized using the conjugate gradient method until the forces are less than 0.1 eVÅ^{-1} (with cell parameters held fixed). The total energy of all structures is first calculated at this DFT-1 level. The most stable structures are then selected for further optimization using the DFT + U ($U_{Ti} = 4.2$ eV) method [38], with an improved k-point sampling (k = 1 x 1 x 3) and larger plane wave basis set (cutoff energy of 350 eV). To ensure consistency, the supercell dimensions are scaled according to the DFT + U bulk rutile lattice constants before optimization (a = 4.668 Å and c = 3.035 Å). Hereafter this second level of DFT optimization is referred to as DFT-2.

In order to compare simulated STEM images with experimentally obtained images, high angle annular dark-field (HAADF) images and annular bright-field (ABF) images for the best possibly optimized GB structure models were calculated by Win-HREM STEM image simulation package (HREM Research Inc.) based on the multi-slice method [45]. The imaging parameters are the same as the experimental conditions (see below). The simulation includes the absorption effect in thermal diffuse scattering for each element.

2.2. Fabrication of samples and STEM imaging

Small angle rutile TiO_2 tilt grain boundaries (GBs) with a deviation angle of 5° were fabricated by solid-state diffusion bonding of two single crystals with high purity. First of all, two TiO_2 crystal blocks were cut along the planes deviating by 2.5° from the (100) planes around the [001] zone axes and then polished by sand paper and fine colloidal silica powder in distilled water. The polished planes were contacted to each other and joined by annealing in air at 1773 K for 10 h. The size of each single crystal is $10 \times 10 \times 5$ mm^3 and hence a 10 mm cubic bicrystal is produced. In order to obtain an ultra-thin cross-sectional TEM sample, the joined block was mechanically cut into 300 μm thick slices and then ground by sand paper and polished by silica powder until the thickness reached around 120 μm, followed by a further dimpling down to around 20 μm. Finally, to make the sample electron transparent, the dimpled samples were thinned by argon-ion sputtering using the PIPS 691 (Gatan Inc.). A gun voltage of 1–4 kV and incident beam angles of 4–6° were used in order to avoid, to the maximum extent, radiation damage to samples.

The structure of the samples were characterized using a conventional TEM JEM-2010F (JEOL Ltd.) and at the atomic scale using a STEM JEM-ARM200F (JEOL Ltd.) with a spherical aberration (Cs) corrector (CEOS GmbH). An acceleration voltage of 200 kV was used, probe convergence semi-angle of 23 mrad, HAADF detector semi-angles of 90–175 mrad, and ABF detector semi-angles of 11–23 mrad. A cold field emission gun (FEG) providing a fine

energy resolution of 0.4 eV and combination with (Gatan Inc.) Enfina system equipped on a STEM revealed a fine structure near the core-loss edge (ELNES) in the electron energy loss spectra.

3. Results

3.1. Experimental

As described in the Methods section we construct low angle bicrystal samples corresponding to 5-degree misorientation about the [001] plane. Conventional TEM imaging (Fig. S1) shows that the bicrystal is well bonded, contains an atomically flat GB with wide area (~100 nm scale) although some GB steps can be seen. The GB consists of a periodic array of edge dislocations which compensate the lattice mismatch caused by 5-degree misorientation about the [001] plane. The separation between edge dislocations at the GB is approximately 3.4 nm (Figs. S1b and c). There is no evidence of secondary phase formation near the GB. The experimental imaging of this dislocation was reported previously but it was not possible there to unambiguously determine its corresponding atomic structure hence the need for a thorough theoretical investigation which is the main focus of the present paper [39,46].

HAADF- and ABF-STEM imaging is used to characterize the atomic scale structure of the dislocations. HAADF-STEM imaging provides Z-contrast sensitivity [47], with the bright spots corresponding to pure Ti atomic columns and darker spots corresponding to the mixed Ti and O atomic columns. On the other hand, ABF-STEM imaging allows for imaging of both light and heavy elements [48]. Therefore, in the case of TiO_2 the pure oxygen columns can also be seen. Fig. 1a and d shows the experimental HAADF-STEM and ABF-STEM images of the dislocation core region. Unfortunately, atomic positions in the inside dislocation core are not as clear as in the bulk. The HAADF intensities of atomic columns near the core region are darker compared to that in the bulk region. This could be caused by distortion of atoms near the dislocation core, bringing atomic columns out of alignment which would affect electron channelling, an effect essential in a typical HAADF imaging. As a result, it is not possible to unambiguously identify the GB plane. We draw two possible Burgers circuits on the experimental images which correspond to the same Burgers vector $\boldsymbol{b} = c[001]$ but are centred on GB planes of different symmetry (GB1 and GB2 in Fig. 1).

Electron energy loss near edge structure (ELNES) spectra from the GBs provide a means to probe the local electronic properties of the dislocation core. Fig. 2 shows the Ti-$L_{2,3}$ edge for a region centred at the dislocation core and away from the core in a bulk-like region. In bulk TiO_2 the Ti-L_3 and the Ti-L_2 edges are split into two e_g and t_{2g} peaks due to the interaction between Ti-3d and O-2p orbitals. The energy of the e_g orbital of the Ti-3d electrons, which is oriented towards the oxygen atoms, is higher than that of the t_{2g} orbital, which is oriented between the oxygen atoms. When an excess electron is donated into TiO_2 localizes on a Ti site forming Ti^{3+}, the energy difference can be reduced due to the relatively isotropic distribution of the additional electron. In the dislocation core region the two peaks in the Ti-L edge spectra are broader than in the bulk suggesting the presence of Ti^{3+} near the dislocation core. The two broad peaks also include a weak shoulder peak denoted by the green arrows in Fig. 2, indicating the presence of a mixture of Ti^{3+} and Ti^{4+} near the dislocation core.

3.2. Predicted dislocation models using classical potential

The system used to model the edge dislocation is shown in Fig. 3. We built a slab with periodic conditions in the $y = [\bar{1}10]$ and $z = [001]$ and free surfaces in the $x = [110]$ direction. The free surfaces of the slab are the stable (110) surfaces [49,50]. An edge dislocation is put at the centre of the slab. It is aligned with the y direction and its Burgers vector is $\boldsymbol{b} = c[001]$. There are 11 layers of unit cells in the z direction for $x < x_{disl}$ (where x_{disl} is the x position of the centre of the dislocation core) and 12 layers for $x > x_{disl}$. The periodic vector of the supercell in the z direction is set to $Z = 11.5 \times c \times [001]$ such that the presence of the dislocation induces an equivalent compressive and tensile strain on both parts of the slab. The periodic vector of the supercell in the y direction is $Y = a \times [\bar{1}10]$. The slab is $5 \times a \times [110]$ thick (prior to surface relaxation). Depending on the stoichiometry of the system, the total number of atoms of the system varies from 689 to 694. The lattice constants are set to those given by the SMTBQ model ($a = 4.615$ Å and $c = 2.982$Å [30]) and are close to the experimental ones ($a = 4.594$ Å and $c = 2.959$Å [51]). Geometry optimizations are performed allowing all atoms within the cell to relax but with the cell dimensions fixed.

We restrained the GO search to dislocation core compositions close to stoichiometry, with an excess/deficiency of oxygen between minus and plus one. Specifically, we considered the following six compositions: $Ti_{230}O_{459}$ ($\Delta O = -1$), $Ti_{231}O_{461}$ ($\Delta O = -1$), $Ti_{230}O_{460}$ ($\Delta O = 0$), $Ti_{231}O_{462}$ ($\Delta O = 0$), $Ti_{230}O_{461}$ ($\Delta O = +1$) and $Ti_{231}O_{463}$ ($\Delta O = +1$), where ΔO is the deviation in the number of oxygen atoms from stoichiometry. For each composition we carried out more than 4000 configuration searches, finding between 72 and 256 distinct stable configurations in each case. The searches were carried out without activating the charge equilibration of the potential. We then selected the configurations having energy within 5 eV of the lowest energy configuration. These configurations were then relaxed including the charge equilibration. Among these relaxed configurations, all those having an energy less than 1 eV larger than the configuration of lowest energy are selected for further study using DFT. Table 1 summarizes the number of configurations obtained for each composition.

3.3. Screening dislocation structures using DFT

The GO above yields a number of prospective stable dislocation structures. We employ two subsequent levels of screening to identify the most stable dislocation structures at the DFT level of theory (see Methods). Table S1 (Supplementary Information) summarizes the total energy for each structure at each level of theory. Calculations are performed at the DFT-1 level on 50 dislocation structures. Subsequent calculations are then performed only on a few of the most stable configurations. For each composition Ti_aO_b we calculate the dislocation formation energy (per unit length) in the following way,

$$E_f(Ti_aO_b) = \frac{E - a\mu_{Ti} - b\mu_O}{L} = \frac{E - a[E(TiO_2) - 2\mu_O] - b\mu_O}{L} \qquad (1)$$

where E is the total energy of the supercell, μ_{Ti} and μ_O are the chemical potentials of Ti and O respectively, L is the length of dislocation in the supercell and $E(TiO_2)$ is the total energy per formula unit of bulk TiO_2. Note that we do not include entropic contributions to the formation energy. Fig. 4 shows how the formation energy varies with oxygen chemical potential for the most stable structures corresponding to each composition Ti_aO_b. We consider the upper limit of oxygen chemical potential to be half the total energy of the oxygen molecule, $\mu_O = \frac{1}{2}E(O_2)$. We note that the relevant lower limit of chemical potential is difficult to define unambiguously as the Ti–O phase diagram includes many sub-stoichiometric phases such as TiO and various Magnélli phases [52,53]. In Fig. 4 we extend the scale to 5 eV below the upper limit (noting that the experimental formation energy of TiO_2 of 4.892 eV

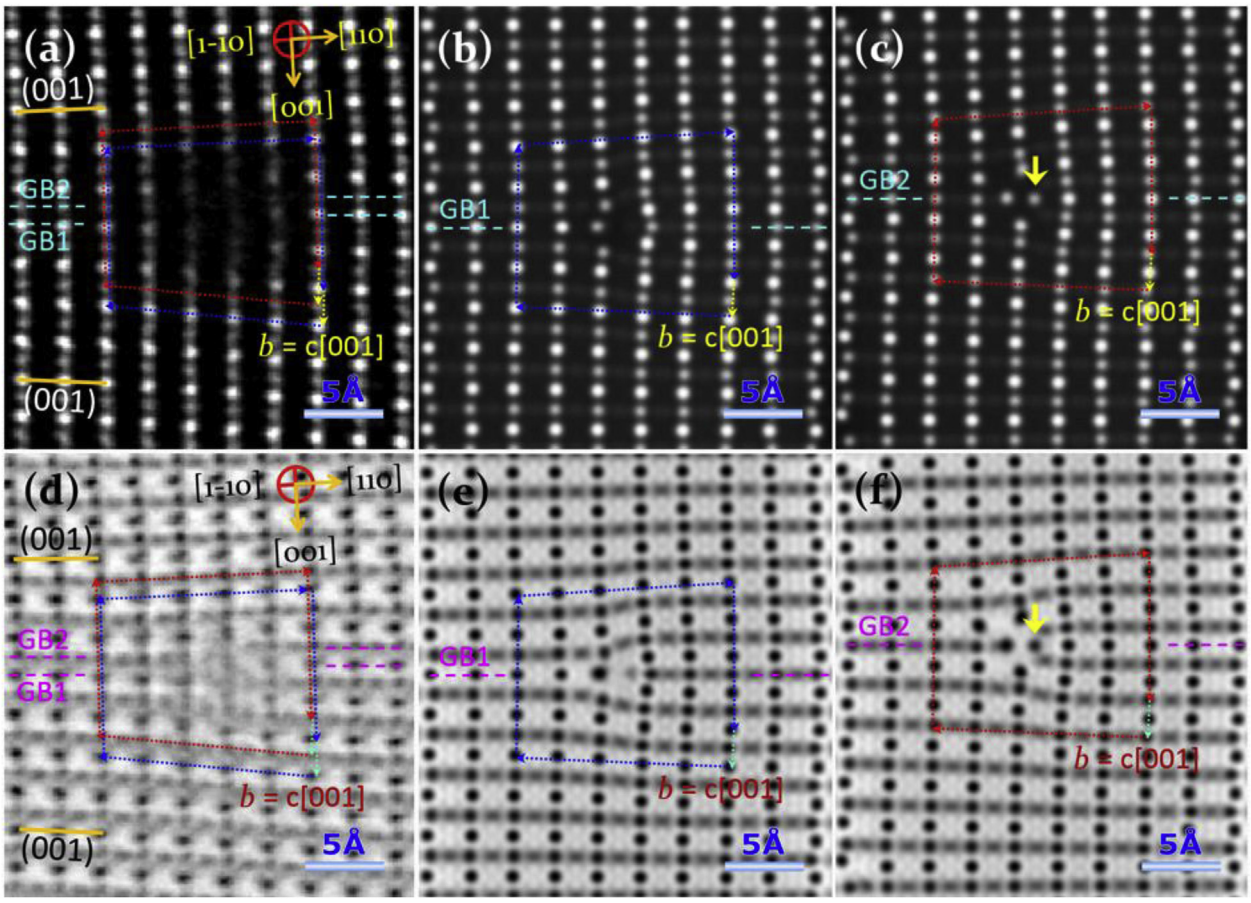

Fig. 1. HAADF-STEM images (top) and ABF-STEM images (bottom) of the b = c[001] edge dislocation in rutile TiO_2. (a)(d) Experimental images, (b)(d) simulated images for the stoichiometric dislocation core model, and (c)(f) simulated images for the highly oxygen deficient dislocation core model. Burgers circuits are also drawn on the images centred on the corresponding GB planes.

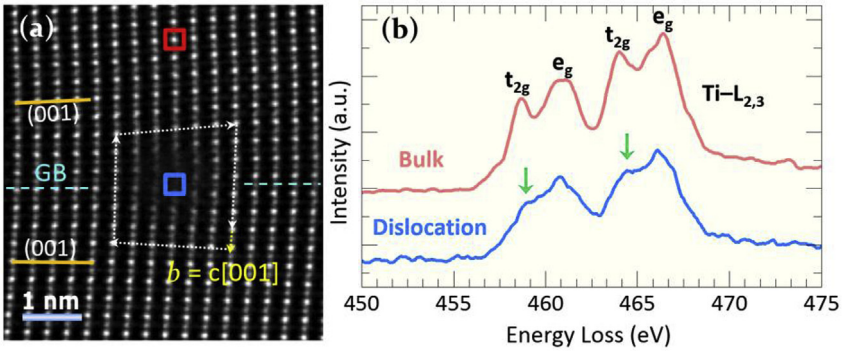

Fig. 2. ELNES profiles of Ti-$L_{2,3}$ edge in a bulk-like region (red) and near the core (blue) of the b = [001] edge dislocation in rutile TiO_2. (b) is reproduced from Ref. [39] with permission from the Royal Society of Chemistry. (For interpretation of the references to colour in this figure legend, the reader is referred to the Web version of this article.)

defines the ultimate limit at which TiO_2 should be reduced to metallic titanium [54]). Over the entire range of oxygen chemical potential, only two of the structures are predicted to be stable ($Ti_{230}O_{460}$ and $Ti_{231}O_{461}$). The former is stoichiometric while the latter is oxygen deficient ($\Delta O = -1$). We note that the most stable oxygen deficient structure actually has a higher density than the most stable stoichiometric structure. A higher density stoichiometric structure was also revealed in our search ($Ti_{231}O_{462}$) but was found to be less stable.

Fig. 5 shows the atomic structure of the two most stable dislocation structures $Ti_{230}O_{460}$ and $Ti_{231}O_{461}$ (hereafter named stoichiometric and oxygen deficient respectively). We note that one cannot simply be considered as a result of removing or adding ions to the other. In other words, a change of stoichiometry causes a significant modification of the structure of the dislocation making this an extremely challenging optimization problem. For analysis of local strain and electronic properties we identify two bulk-like regions (B^1 and B^2) and the dislocation core region (D) in Fig. 5. For both the stoichiometric and oxygen deficient dislocation structure region B^2 is the most similar to the bulk crystal structure. In

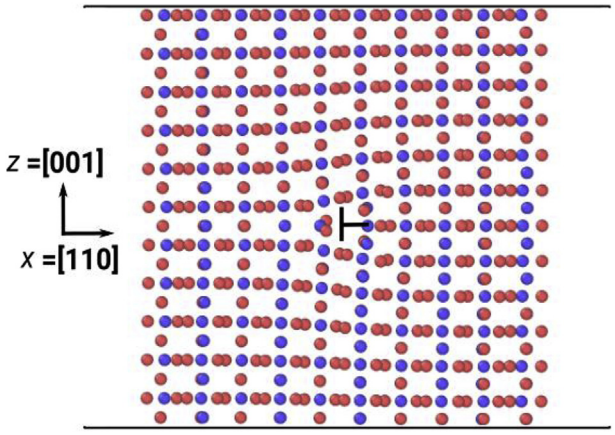

Fig. 3. The slab with periodic boundary conditions in the $\boldsymbol{z} = [001]$ and $\boldsymbol{y} = [\bar{1}10]$ directions used to model the $b = c[001]$ edge dislocation core.

cores and highlight the corresponding GB plane to compare to the experimental STEM images (Fig. 1a and b). It is interesting to note that the stoichiometric dislocation core model has a GB plane corresponding to GB1 in the experimental image while the oxygen deficient dislocation has a GB plane corresponding to GB2. A plausible interpretation for the poor experimental STEM contrast in the core region is that the dislocation has variable stoichiometry in the projection direction hence could be considered as a superposition of the stochiometric and oxygen deficient models. We discuss this further in the Discussion section below.

3.4. Predicted electronic properties of TiO_2 dislocations

Fig. 6a shows the calculated electronic density of states for the stoichiometric and oxygen deficient dislocation. For the stoichiometric dislocation we find the region that is most bulk-like (B^2) has a very similar electronic structure and band gap to that predicted for the ideal bulk crystal. Therefore, in the following we use B^2 as a reference for the bulk electronic structure. Region B^1, which is more highly strained, has a similar band gap but is downshifted by about 0.2 eV with respect to B^2. The dislocation core region D is associated with a band of unoccupied states extending 0.3 eV below the bulk conduction band minimum. However, there are no occupied states associated with the dislocation core that extend above the bulk valence band maximum. This suggests that the dislocation may act as a trap for photoexcited electrons but not holes.

Analysis of the electronic structure for the oxygen deficient dislocation reveals a more complex picture. The most bulk-like (B^2) region again has similar electronic structure and band gap to that predicted for the ideal bulk crystal and no states in the gap. However, in the dislocation core region (D), there are occupied electronic states close to the bulk valence band maximum (see Fig. 6b). These states are associated with localized electrons (Ti^{3+} sites) trapped near the core that are donated into the dislocation as a result of the oxygen deficiency. Normally electrons donated by vacancies in TiO_2 localize on Ti ions in relatively shallow levels (<1eV below the conduction band edge). In the case of the dislocation the electrons are trapped much more strongly and the levels are so low in the gap they are close to the valence band maximum. To provide insight into the location of localized electrons in the oxygen deficient dislocation structure we show the corresponding spin-density isosurface in Fig. 7. Two distinct localized electrons (each with opposite spin) can be identified from the isosurface with characteristic *d*-orbital symmetry. Since the dislocation is one oxygen atom short of stoichiometry the presence of two electrons is consistent with the vacancy donating two localized electrons as expected. The distortion accompanying electron localization in bulk rutile TiO_2 involves outward relaxation of the six neighbouring oxygen ions leading to Ti–O bonds of around 2.1 Å in length (e.g. see Refs. [22,49]). The distortion around the Ti^{3+} species at the

Table 1
Summary of the core configuration search from the classical potential. $n_{searches}$ is the number of configuration searches. n_{config} is the number of configurations found, $n_{config,\ E<Emin+5}$ is the number of configurations which have an energy less than 5 eV higher than the configuration with the lowest energy. $n_{config,\ E<Emin+1}$ is the number of configurations which after relaxation with charge equilibration have an energy less than 1 eV higher than the configuration with the lowest energy.

Composition	$n_{searches}$	n_{config}	$n_{config,\ E<Emin+5}$ (without charge equilibration)	$n_{config,\ E<Emin+1,}$ (with charge equilibration)
$Ti_{230}O_{459}$	7700	256	74	9
$Ti_{231}O_{461}$	8062	186	7	4
$Ti_{230}O_{460}$	7380	78	14	6
$Ti_{231}O_{462}$	4122	244	11	4
$Ti_{230}O_{461}$	4226	232	10	6
$Ti_{231}O_{463}$	14387	72	40	21

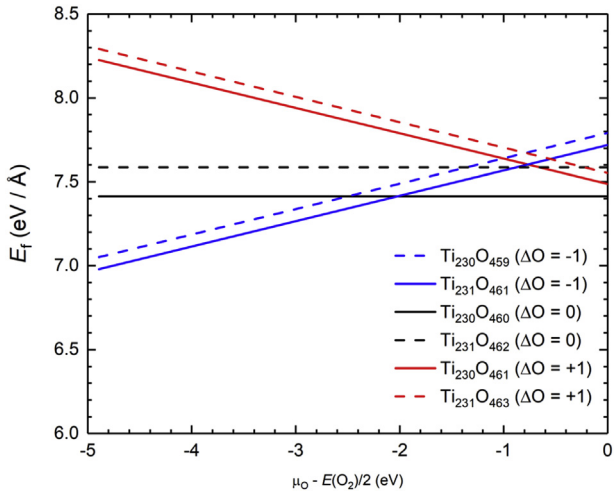

Fig. 4. Formation energy of the most stable predicted dislocation structures as a function of oxygen chemical potential - see Eq. (1) in the text.

particular for the stoichiometric structure region B^2 has only −0.3% and +2.9% strain in the [110] and [001] directions respectively. For the oxygen deficient structure, the strain in region B^2 is +0.3% and +2.7% in the [110] and [001] directions respectively. Region B^1 in both structures have a more significant compressive strain in the [001] direction (between −4.6 and −7.0%) accompanied by a corresponding dilation in the [110] direction.

To compare the predicted dislocation structures against the experimental images we performed image contrast simulations for the DFT optimized stoichiometric and oxygen deficient models (Fig. 1b,c, e, and f). We draw Burgers circuits around the dislocation

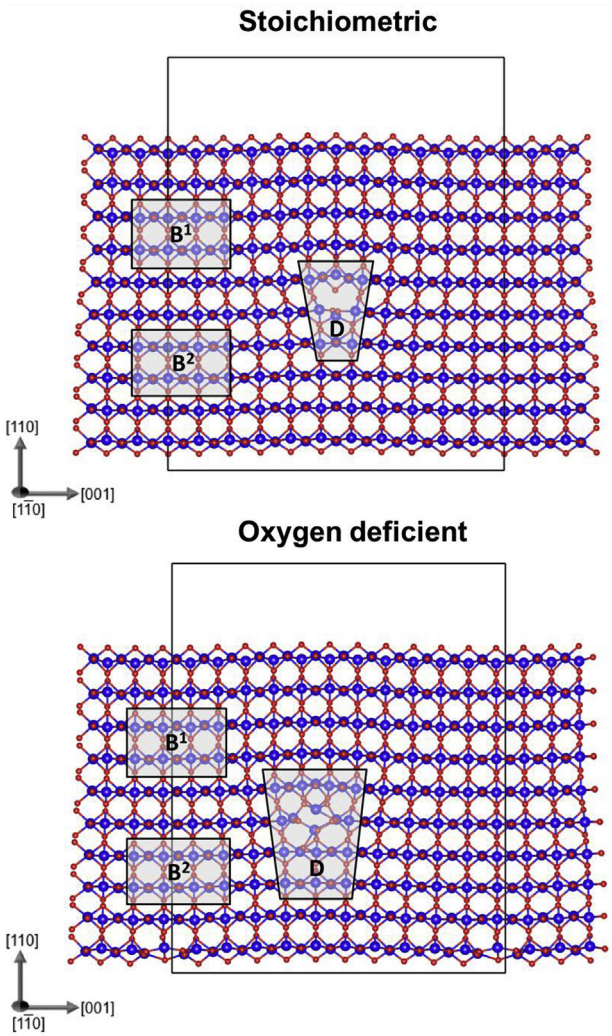

Fig. 5. Predicted structure of the stoichiometric ($Ti_{230}O_{460}$) and oxygen deficient ($Ti_{231}O_{461}$) dislocation. Titanium and oxygen ions are shown as blue and red spheres respectively. Bulk-like regions (B^1 and B^2) and the dislocation core region (D) are highlighted and their local strain and electronic properties are discussed in the text. (For interpretation of the references to colour in this figure legend, the reader is referred to the Web version of this article.)

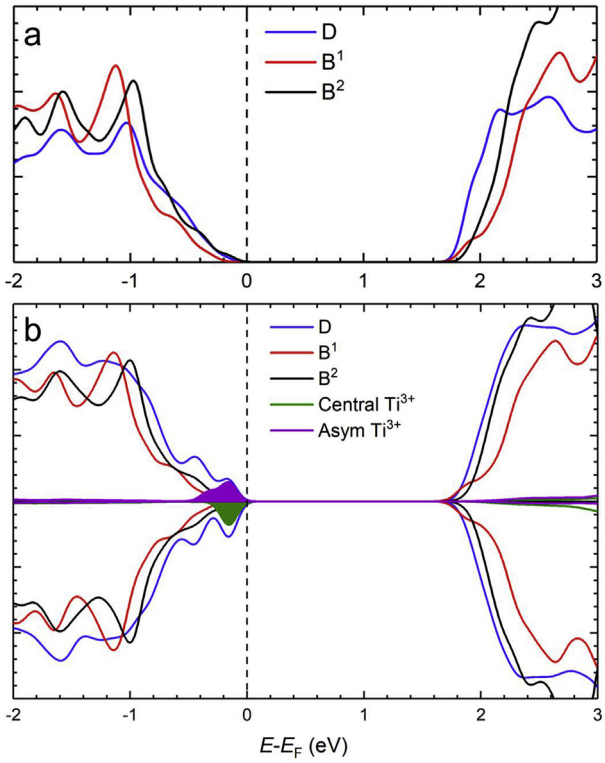

Fig. 6. Calculated projected density of states for a) stoichiometric and b) oxygen deficient dislocation structures. The Fermi energy is taken as the zero of the energy scale. The density of states is projected onto atoms in different regions as indicated in Fig. 5. For the oxygen deficient dislocation the projected density of states on the central and asymmetrically located Ti^{3+} sites (see Fig. 5) are also shown.

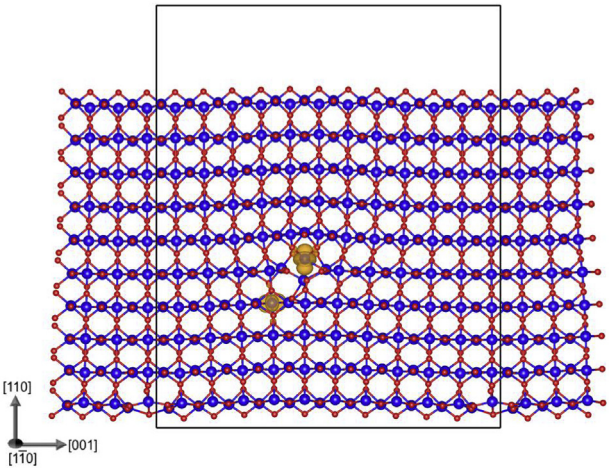

Fig. 7. Electron spin density isosurface (orange) highlighting the location of localized electrons (Ti^{3+}) in the vicinity of the oxygen deficient dislocation structure. Titanium and oxygen ions are shown as blue and red spheres respectively. (For interpretation of the references to colour in this figure legend, the reader is referred to the Web version of this article.)

dislocation is much stronger and also highly asymmetric. While many of the bonds are also around 2.1 Å, a few are much longer (up to 2.5 Å). This difference gives these sites a much more favourable electrostatic potential for electron localization. This analysis suggests it is the local geometry of Ti ions at the dislocation (in particular, their extended Ti—O bonds) that make them preferential sites for localization of electrons. The predicted formation of Ti^{3+} sites near the oxygen deficient dislocation core is consistent with the experimental EELS characterization of the $\boldsymbol{b} = c[001]$ edge dislocation discussed in Sec. 3.1.

4. Discussion

We now discuss some of the factors that may affect the accuracy of our predictions and experimental observations as well as the agreement between them. We first address the theoretical predictions.

Due to the vast configuration space of the dislocation (both in terms of atomic structure and composition) it is not feasible to perform the global optimization fully at the quantum mechanical level. Our multilevel approach uses the SMTBQ potential at the first stage where over 1000 different configurations have been considered before assessing the stability of the most stable structures at both standard DFT and DFT + U levels of theory. The SMTBQ potential has been developed to provide an improved description of low symmetry defects (such as steps on TiO_2 surfaces [30]) and includes charge transfer effects. It should, therefore, provide a good

balance between accuracy and computational cost. The DFT and DFT + U levels of theory provide more sophisticated descriptions and importantly allow access to the electronic structure of the system. We employ a large supercell (about 690 atoms) to minimize artificial effects arising from the confinement of the dislocation strain field in a periodic supercell. While such effects are not completely eliminated, we are able to define a bulk-like region away from the dislocation core that is within 3% of the crystal lattice constants providing a reference for comparing bulk and dislocation core properties. As discussed in Sec. 2.1 all calculations are performed assuming charge neutrality. Since the dislocation defects do not introduce unoccupied electronic states inside the gap and TiO_2 is an intrinsic n-type semiconductor (with the Fermi energy near the conduction band minimum) the assumption that the neutral charge state of the dislocation is the most stable one appears to be reasonable.

In comparing the relative stability of dislocation structures across the three levels of theory some notable difference in relative stability can be observed. One should expect that DFT and DFT + U should give consistent descriptions for stoichiometric structures. However, for oxygen deficient structures in rutile the localization of the donated electrons is known to be incorrectly described by DFT as a result of the self-interaction error. DFT + U should give a more reasonable description in these cases. This expectation is reflected in the results shown in Table S1. For the stoichiometric structures ($Ti_{230}O_{460}$ and $Ti_{231}O_{462}$) both DFT and DFT + U agree on the most stable structure. For the oxygen deficient structures there is a large (>1.3 eV difference in relative stability) disagreement between DFT and DFT + U and the latter is expected to be more accurate for the reason discussed above. Both DFT and DFT + U agree that the oxygen rich structures are not stable across the relevant range of chemical potential (shown in Fig. 2) but there are differences in stability between DFT and DFT + U for some structures (although smaller at < 0.6 eV). In summary, since DFT + U provides a better description than DFT for the oxygen deficient structures we believe it is the more reliable method to make the final assessment of relative stability and electronic properties. One well known shortcoming of the DFT + U approach is that it gives an underestimate of the band gaps of TiO_2 crystals. A hybrid functional approach like the one recently developed to model polarons in bulk TiO_2 phases could provide more accurate predictions of electronic structure but would come at increased computational cost due to the large supercells that are required [22].

We now discuss the experimental results reported in Section 3.1. As noted above it is notable that the HAADF- and ABF-STEM contrast in the central core region is not as good as away from the dislocation core. While the images clearly show the presence of the dislocation core and its symmetry, the exact position of atoms inside the core is more difficult to pinpoint. One of the effects that can give rise to this sort of contrast is site-to-site variation in atom displacements along the projection direction. The TEM samples are 5–15 nm thick and therefore the images are formed by electron transmission through many atomic layers. Local variations in composition along the projection direction, or the presence of impurities of defects segregated to the core will affect local atomic displacements and bring atoms in columns out of alignment. It is also possible that the atoms near the upper and lower free surfaces of the samples may be distorted differently in the centre of the sample. However, the STEM samples are quite thick (around 10 nm) in comparison to the expected region of surface distortion (around 0.4 nm). Since the image contrast is formed by interaction of the electron beam with the entire volume we would expect the surface effect to be insufficient to explain the observed contrast near the core. Indeed, STEM images for other types of extended defects we have studied employing similar samples do not show such strong distortions at the interface [55]. Therefore, we believe the observed distortions more likely represent deviations in atom positions along the entire dislocation line (not just at the surface). These types of distortion are likely to be more pronounced at the dislocation core owing to its reduced symmetry and ion coordination and will have a negative impact on electron channelling and hence reduce contrast. For this reason, experimental imaging alone is often insufficient to fully resolve the atomic structure of a dislocation in a complex material such as TiO_2, hence complementary theoretical modeling is essential.

Our comparison between the predicted models (both stoichiometric and oxygen deficient) and the experimental images shows that both are plausible models. The EELS results show a clear difference between the dislocation and the bulk regions and suggest the presence of reduced Ti in the core, in line with the predictions for the oxygen deficient model. We do not attempt here a quantitative simulation of the EEL spectra which would be extremely challenging for a supercell of this size however the predicted spin density of the oxygen deficient model is consistent with the experimental observation. Based on the above discussion we propose that it is quite likely that along the projection direction there may be sections of the dislocation core that are stoichiometric and other parts that are oxygen deficient giving rise to inhomogeneous distortions explaining both the reduced contrast near the core and the presence of Ti^{3+} detected by EELS. Even for a homogeneous oxygen deficient dislocation the localization of electrons at different sites equivalent by symmetry (see Fig. 7) could also give rise to small distortions along the dislocation core.

5. Conclusions

To summarize, we have performed a theoretical investigation into the structure and properties of the $\boldsymbol{b} = c[001]$ edge dislocation in rutile TiO_2 combining both second moment tight binding charge transfer model and density functional levels of theory within a global optimization framework. The results indicate that both stoichiometric and substoichiometric dislocation cores can be stable depending on the oxygen chemical potential. The latter is associated with electrons localized on Ti sites near the core (Ti^{3+}) with corresponding electronic states that are close to the valence band maximum. These predictions are consistent with experimental images of the dislocation core structure obtained using HAADF- and ABF-STEM and the bicrystal approach. Furthermore, EELS provides evidence for reduced Ti sites in the core region consistent with the predicted electronic properties of the substoichiometric dislocation core. Experimentally, the contrast in the central core region is observed to be weaker than in the bulk and we suggest this can be understood as a result of local variation in dislocation stoichiometry along the incoming beam direction which would result in distortion of atoms away from perfect atomic column registry.

Predicting the structure of dislocations in a complex compound semiconductor such as TiO_2 is an extremely challenging problem owing to the vast phase space of atomic structures and compositions. On the other hand, imaging is also challenging making direct experimental determinations of structures and properties difficult. Here we have demonstrated how the combination of several levels of theory within a global optimization framework can reveal stable atomic structures that are consistent with experiment and in doing so provide atomic scale insight into their electronic properties. Specifically, we have shown that both stoichiometric and oxygen deficient edge dislocations in rutile TiO_2 can be stable, depending on the oxygen chemical potential. The oxygen deficient dislocation is associated with Ti^{3+} states which are close to the valence band maximum and localized in the core region. Both dislocations can

have a propensity to trap electrons but not holes, suggesting they do not act as strong recombination centers. Altogether this study provides atomistic insight of relevant to applications of TiO_2 in resistive switching memories, solar cells and photocatalysis [23,24]. Furthermore, the approach we have employed could be used in the modeling of the structure and properties of other complex defects such as GBs, antiphase boundaries and surface reconstructions in a much wider range of materials [55–57].

Contributions

E.M. performed the global optimization calculations using the tight binding charge transfer model supervised by H.J. M.S. carried out experiments and K.I. discussed the results under the direction of Y.I. K.M. performed the density functional theory calculations and wrote the manuscript with input from all co-authors.

Conflicts of interest

The authors declare no competing interests.

Acknowledgements

K.P.M. acknowledges support from EPSRC (EP/K003151/1, EP/P006051/1 and EP/P023843/1). This work made use of the facilities of Archer, the UK's national high-performance computing service, via our membership in the UK HPC Materials Chemistry Consortium, which is funded by EPSRC (EP/L000202/1). This study is partly supported by Grant-in-Aid for Specially Promoted Research (No. JP17H06094) from Japan Society for the Promotion of Science, and “Nanotechnology Platform” (Project No. 12024046) from the Ministry of Education, Culture, Sports, Science and Technology, Japan. All data relating to the theoretical calculations created during this research are available by request from the University of York Research database https://doi.org/10.15124/ee8404f9-9b3d-41ec-92cc-44baf9b9382e. We thank R. Sun for useful discussions.

Appendix A. Supplementary data

Supplementary data to this article can be found online at https://doi.org/10.1016/j.actamat.2018.10.015.

References

[1] V. Celli, et al., Theory of dislocation mobility in semiconductors, Phys. Rev. 131 (1) (1963) 58–72.
[2] N. Shibata, et al., Nonstoichiometric dislocation cores in α-alumina, Science 316 (5821) (2007) 82.
[3] D.L. Dexter, F. Seitz, Effects of dislocations on mobilities in semiconductors, Phys. Rev. 86 (6) (1952) 964–965.
[4] J.R.K. Bigger, et al., Atomic and electronic structures of the 90 degree partial dislocation in silicon, Phys. Rev. Lett. 69 (15) (1992) 2224–2227.
[5] K.P. McKenna, Electronic and chemical properties of a surface-terminated screw dislocation in MgO, J. Am. Chem. Soc. 135 (50) (2013) 18859–18865.
[6] Z. Wang, et al., Polymorphism of dislocation core structures at the atomic scale, Nat. Commun. 5 (2014) 3239.
[7] K. Otsuka, et al., Dislocation-enhanced ionic conductivity of yttria-stabilized zirconia, Appl. Phys. Lett. 82 (6) (2003) 877–879.
[8] G.R. Love, Dislocation pipe diffusion, Acta Metall. 12 (6) (1964) 731–737.
[9] S. Tomoya, et al., Direct evidence that dislocations are non-radiative recombination centers in GaN, Jpn. J. Appl. Phys. 37 (4A) (1998) L398.
[10] D. Blavette, et al., Three-Dimensional atomic-scale imaging of impurity segregation to line defects, Science 286 (5448) (1999) 2317.
[11] L. Sun, D. Marrocchelli, B. Yildiz, Edge dislocation slows down oxide ion diffusion in doped CeO_2 by segregation of charged defects, Nat. Commun. 6 (2015) 6294.
[12] T. Wosiński, Evidence for the electron traps at dislocations in GaAs crystals, J. Appl. Phys. 65 (4) (1989) 1566–1570.
[13] Y. Chen, et al., Luminescence in deformed MgO, CaO and SrO, Philos. Mag. A: A Journal of Theoretical Experimental and Applied Physics 32 (1) (1975) 99–112.
[14] P.M. Petroff, L.C. Kimerling, Dislocation climb model in compound semiconductors with zinc blende structure, Appl. Phys. Lett. 29 (8) (1976) 461–463.
[15] A. Seidl, et al., Generalized Kohn-Sham schemes and the band-gap problem, Phys. Rev. B 53 (7) (1996) 3764–3774.
[16] R. Haunschild, et al., Many-electron self-interaction and spin polarization errors in local hybrid density functionals, J. Chem. Phys. 133 (13) (2010) 134116.
[17] E.A. Carter, Challenges in modeling materials properties without experimental input, Science 321 (5890) (2008) 800.
[18] K.C. Ko, et al., Performance of a modified hybrid functional in the simultaneous description of stoichiometric and reduced TiO_2 polymorphs, Phys. Chem. Chem. Phys. 18 (17) (2016) 12357–12367.
[19] F. Viñes, et al., Systematic study of the effect of HSE functional internal parameters on the electronic structure and band gap of a representative set of metal oxides, J. Comput. Chem. 38 (11) (2017) 781–789.
[20] C. Di Valentin, G. Pacchioni, A. Selloni, Reduced and n-type doped TiO_2: nature of Ti^{3+} species, J. Phys. Chem. C 113 (48) (2009) 20543–20552.
[21] M. Setvin, et al., Direct view at excess electrons in TiO_2 rutile and anatase, Phys. Rev. Lett. 113 (8) (2014), 086402.
[22] A.R. Elmaslmane, M.B. Watkins, K.P. McKenna, First-Principles modeling of polaron formation in TiO_2 polymorphs, J. Chem. Theor. Comput. 14 (7) (2018) 3740–3751.
[23] R. Waser, M. Aono, Nanoionics-based resistive switching memories, Nat. Mater. 6 (2007) 833.
[24] F. Spadavecchia, et al., Solar photoactivity of nano-N-TiO_2 from tertiary amine: role of defects and paramagnetic species, Appl. Catal. B Environ. 96 (3) (2010) 314–322.
[25] K.H.G. Ashbee, R.E. Smallman, Stress-strain behavior of titanium dioxide (rutile) single crystals, J. Am. Ceram. Soc. 46 (5) (1963) 211–214.
[26] W.M. Hirthe, J.O. Brittain, Dislocations in rutile as revealed by the Etch-Pit technique, J. Am. Ceram. Soc. 45 (11) (1962) 546–554.
[27] R.L. Penn, J.F. Banfield, Imperfect oriented attachment: dislocation generation in defect-free nanocrystals, Science 281 (5379) (1998) 969.
[28] K.K. Adepalli, et al., Influence of line defects on the electrical properties of single crystal TiO2, Adv. Funct. Mater. 23 (14) (2012) 1798–1806.
[29] S.I. Cha, et al., Crystal splitting and enhanced photocatalytic behavior of TiO2 rutile nano-belts induced by dislocations, Nanoscale 5 (2) (2013) 753–758.
[30] E. Maras, et al., Improved tight-binding charge transfer model and calculations of Energetics of a step on the rutile TiO_2(110) surface, J. Phys. Chem. C 119 (19) (2015) 10391–10399.
[31] G. Sattonnay, R. Tétot, Bulk, surface and point defect properties in UO_2 from a tight-binding variable-charge model, J. Phys. Condens. Matter 25 (12) (2013) 125403.
[32] R. Tétot, et al., Tight-binding variable-charge model for insulating oxides: application to TiO_2 and ZrO_2 polymorphs, EPL (Europhysics Letters) 83 (4) (2008) 40001.
[33] R. Tétot, et al., $SrTiO_3$ (001) surface and strained thin films: atomic simulations using a tight-binding variable-charge model, Surf. Sci. 616 (2013) 19–28.
[34] G. Henkelman, H. Jónsson, A dimer method for finding saddle points on high dimensional potential surfaces using only first derivatives, J. Chem. Phys. 111 (15) (1999) 7010–7022.
[35] A. Pedersen, J.C. Berthet, H. Jónsson, Simulated annealing with coarse graining and distributed computing, Lecture Notes in Computer Science, in: Applied Parallel and Scientific Computing. PARA, vol. 7134Springer, Berlin, Heidelberg, 2010. Applied Parallel and Scientific Computing. PARA 2010., K. Jónasson, Editor. 2012, Springer, Berlin, Heidelberg.
[36] M. Plasencia, et al., Geothermal model calibration using a global minimization algorithm based on finding saddle points and minima of the objective function, Comput. Geosci. 65 (2014) 110–117.
[37] M. Plasencia Gutiérrez, C. Argáez, H. Jónsson, Improved minimum mode following method for finding first order saddle points, J. Chem. Theor. Comput. 13 (1) (2017) 125–134.
[38] S.L. Dudarev, et al., Electron-energy-loss spectra and the structural stability of nickel oxide: an LSDA+U study, Phys. Rev. B 57 (3) (1998) 1505–1509.
[39] R. Sun, et al., A dislocation core in titanium dioxide and its electronic structure, RSC Adv. 5 (24) (2015) 18506–18510.
[40] Y. Ikuhara, Nanowire design by dislocation technology, Prog. Mater. Sci. 54 (6) (2009) 770–791.
[41] S.T. Chill, et al., EON : software for long time simulations of atomic scale systems, Model. Simulat. Mater. Sci. Eng. 22 (5) (2014), 055002.
[42] G. Kresse, J. Furthmüller, Efficiency of ab-initio total energy calculations for metals and semiconductors using a plane-wave basis set, Comput. Mater. Sci. 6 (1) (1996) 15–50.
[43] G. Kresse, J. Furthmüller, Efficient iterative schemes for ab initio total-energy calculations using a plane-wave basis set, Phys. Rev. B 54 (16) (1996) 11169–11186.
[44] J.P. Perdew, K. Burke, M. Ernzerhof, Generalized gradient approximation made simple, Phys. Rev. Lett. 77 (18) (1996) 3865–3868.
[45] K. Ishizuka, N. Uyeda, A new theoretical and practical approach to the multislice method, Acta Crystallogr. A 33 (5) (1977) 740–749.
[46] R. Sun, Grain Boundaries and Dislocations of Titanium Dioxide, University of Tokyo, 2015.
[47] S.J. Pennycook, L.A. Boatner, Chemically sensitive structure-imaging with a scanning transmission electron microscope, Nature 336 (1988) 565.

[48] S.D. Findlay, et al., Robust atomic resolution imaging of light elements using scanning transmission electron microscopy, Appl. Phys. Lett. 95 (19) (2009) 191913.
[49] S.K. Wallace, K.P. McKenna, Facet-dependent electron trapping in TiO_2 nanocrystals, J. Phys. Chem. C 119 (4) (2015) 1913–1920.
[50] V.E. Henrich, P.A. Cox, The Surface Science of Metal Oxides, Cambridge University Press, 1996.
[51] C.J. Howard, T.M. Sabine, F. Dickson, Structural and thermal parameters for rutile and anatase, Acta Crystallogr. B B47 (1991) 462–468.
[52] J.L. Murray, H.A. Wriedt, The O–Ti (Oxygen-Titanium) system, J. Phase Equil. 8 (1987) 148.
[53] L. Liborio, N. Harrison, Thermodynamics of oxygen defective Magneli phases in rutile: a first-principles study, Phys. Rev. B 77 (10) (2008) 104104.
[54] G.L. Humphrey, The heats of formation of TiO, Ti_2O_3, Ti_3O_5 and TiO_2 from combustion calorimetry, J. Am. Chem. Soc. 73 (4) (1951) 1587–1590.
[55] K.P. McKenna, et al., Atomic-scale structure and properties of highly stable antiphase boundary defects in Fe_3O_4, Nat. Commun. 5 (2014) 5740.
[56] A. Vittadini, M. Casarin, A. Selloni, Chemistry of and on TiO_2-anatase surfaces by DFT calculations: a partial review, Theoretical Chemistry Accounts 117 (5) (2007) 663–671.
[57] A.M. van der Zande, et al., Grains and grain boundaries in highly crystalline monolayer molybdenum disulphide, Nat. Mater. 12 (2013) 554.